

Spectral unmixing of hyperspectral imagery for mineral exploration: comparison of results from SFSI and AVIRIS

R.A. Neville, J. Lévesque, K. Staenz, C. Nadeau, P. Hauff, and G.A. Borstad

Abstract. Hyperspectral image data sets acquired near Cuprite, Nevada, in 1995 with the Short-Wave Infrared (SWIR) Full Spectrum Imager (SFSI) and in 1996 with the Airborne Visible–Infrared Imaging Spectrometer (AVIRIS) are analysed with a spectral unmixing procedure and the results compared. The nominal pixel centre spacings are 1.0 by 1.5 m for SFSI and 16.2 by 18.1 m for AVIRIS across track and along track, respectively; the region imaged by SFSI is a small portion of the full AVIRIS scene. Both data cubes have nominal spectral band centre spacings of approximately 10 nm. The image data, converted to radiance units, are atmospherically corrected and converted to surface reflectances. Spectral end members are extracted automatically from the two data sets; those representing mineral species common to both are compared to each other and to reference spectra obtained with a field instrument, the Portable Infrared Mineral Analyser (PIMA). The full sets of end members are used in a constrained linear unmixing of the respective hyperspectral image cubes. The resulting unmixing fraction images derived from the AVIRIS and SFSI data sets for the minerals alunite, buddingtonite, kaolinite, and opal correlate well, with correlation coefficients ranging from 0.75 to 0.91, after compensation for shadowing and misregistration effects.

Résumé. Des ensembles de données hyperspectrales acquises près de Cuprite, au Nevada, en 1995 avec l'imageur SFSI (short-wave infrared full spectrum imager) et en 1996 avec le capteur AVIRIS (airborne visible–infrared imaging spectrometer) sont analysés à l'aide d'une procédure de démixage spectral et les résultats sont comparés. L'espacement des centres de pixels est de 1,0 m par 1,5 m pour SFSI et de 16,2 m par 18,1 m pour AVIRIS respectivement en visée latérale et longitudinale; la région imagée par SFSI est une petite portion de la scène AVIRIS complète. Les deux cubes de données ont un espacement de centres de bandes spectrales d'environ 10 nm. Les données images, converties en unités de luminance, sont soumises à une correction atmosphérique et converties en réflectance de surface. Des composantes spectrales homogènes sont extraites automatiquement des deux ensembles de données; celles qui représentent des espèces minérales communes aux deux ensembles sont comparées l'une à l'autre et par rapport à des spectres de référence obtenus à l'aide d'un instrument de terrain, le PIMA (portable infrared mineral analyser). Les ensembles complets de composantes spectrales homogènes sont utilisés dans une procédure de démixage spectral à contrainte linéaire des cubes d'images hyperspectrales respectifs. Les images des fractions de composantes résultant du démixage dérivées des ensembles de données AVIRIS et SFSI pour les minéraux comme l'alunite, la buddingtonite, la kaolinite et l'opale montrent une bonne corrélation, avec des coefficients de corrélation variant de 0,75 à 0,91, après compensation pour les effets d'ombre et les défauts de superposition. [Traduit par la Rédaction]

Introduction

The use of spectral reflectance measurements in the Short-Wave Infrared (SWIR) part of the electromagnetic spectrum to identify minerals in the field is becoming fairly common. These measurements can be made with one of a number of commercially available portable field spectrometers. Libraries of reference spectra are available against which the field data can be correlated and classified. This technique has been extended by mounting a spectrometer in an aircraft so that much more extensive surveys can be undertaken. These airborne instruments can be designed to collect images in many narrow contiguous wavelength bands; such instruments are known as imaging spectrometers (Borstad et al., 1985; Porter and Enmark, 1987; Vane and Goetz, 1988; Neville and Powell, 1992) and are capable of measuring spectra in more than 100 bands for tens of thousands of target points per second. Two such instruments are the Airborne Visible–Infrared Imaging

Spectrometer (AVIRIS) (Green et al., 1998) and the SWIR Full Spectrum Imager (SFSI) (Neville et al., 1995). The first, developed and operated by the National Aeronautics and Space Administration (NASA), has been instrumental in providing data sets over various targets for the purpose of developing

Received 5 April 2002. Accepted 19 September 2002.

R.A. Neville¹ and K. Staenz. Canada Centre for Remote Sensing, Natural Resources Canada, 588 Booth Street, Ottawa, ON K1A 0Y7, Canada.

J. Lévesque. Defence Research and Development Canada – Valcartier, Val-Bélair, QC G3J 1X5, Canada.

C. Nadeau. MacDonald Dettwiler and Associates, Richmond, BC V6V 2J3, Canada.

P. Hauff. Spectral International Inc., Arvada, CO 80001, U.S.A.

G.A. Borstad. G.A. Borstad Associates Ltd., Sidney, BC V8L 5Y8, Canada.

¹Corresponding author (e-mail: robert.neville@ccrs.nrcan.gc.ca).

methods and applications for imaging spectrometry. The second, developed by the Canada Centre for Remote Sensing (CCRS) for research purposes, has undergone recent modifications to adapt it for survey use and is currently available commercially for general use.

Any one of the growing number of airborne imaging spectrometers can provide very large volumes of data in relatively short time periods. The challenge to those researchers working in imaging spectrometry has been the development of techniques to process and analyse these data in a timely fashion while taking care to extract all the information of interest. One of the methods that has attracted considerable interest is spectral unmixing (Adams et al., 1986; Boardman, 1989; 1990).

It has long been understood by many in the remote sensing community that the radiance collected from a spatial element, represented by an image pixel, rarely comes from a single target material. This is especially true if the target is a natural one as compared to a cultural one. Nearly all pixel radiances consist of light reflected from a number of different target materials or components. The larger the pixel footprint, the less likely it will consist of a pure material. Even when the instantaneous field-of-view (FOV) of the sensor is filled by a single target material, mixing of radiance from adjacent pixels can occur because of atmospheric scattering. Thus, when one attempts to use spectrometric methods to identify the material represented by an image pixel, one is forced to contend with the fact that the measured spectrum has been created by a mixture of materials.

It is most often assumed that the reflected radiances from the pure materials combine linearly, i.e., that the spectral radiance for the mixture is simply the sum of the radiances from each of the constituents. In one sense this is always true, provided that the interaction with the atmosphere is excluded: the radiance reaching the sensor is the sum of the radiance components that left the individual elements of the target. However, the spectrum of the radiance component leaving a given target element may not be characteristic solely of the material of which that element is comprised. Physically this arises when the radiance has interacted with more than one target constituent prior to being captured by the sensor. This is the case for targets such as vegetation, where the radiation cascades from one canopy layer to the next and to the ground, and then is reflected back through the various layers up to the sensor. A similar process occurs as light interacts with a column of water. As the radiance transits each layer, its spectrum is modified by absorption within that layer, thereby taking on the spectral characteristics, at least in part, of each of the layers in sequence. This process is inherently nonlinear. The same can occur when the incident solar irradiance is reflected from one constituent to another before being reflected toward the sensor. It may also occur where minerals are "intimately" mixed such that the radiation traverses a crystal of one mineral, enters a neighbouring crystal of another mineral, and subsequently is scattered toward the sensor. If the atmosphere is included in the discussion, then one could conclude that all the radiation

detected by the sensor has undergone a nonlinear mixing process, this by virtue of the fact that the solar irradiance interacts with, in sequence, the atmosphere, the target, and then the atmosphere again. In this case there are a number of techniques (Staez and Williams, 1997; Tanré et al., 1990; Teillet and Santer, 1991; Berk et al., 1993; Anderson et al., 1995) that have been developed solely to correct for the effects of the atmosphere.

Notwithstanding all of the foregoing examples of physical situations in which spectral mixing is inherently nonlinear, we shall assume a linear mixing model for the present work. Validation efforts (to be reported in a future publication) involving one of the data sets used in the current study lead one to expect that a linear model will give satisfactory results for the type of target examined in the present work. Following the previous discussion on nonlinear mixing, one can extend this statement to all terrestrial targets in which there is no significant vegetation and little intimate mixing of different species within the target material.

The principal objective of this study is to determine the robustness of the spectral unmixing processing methodology by applying it to two different data sets, collected over the same target, one by a low-flying, high spatial resolution SFSI, the other by a high-flying, low spatial resolution AVIRIS. In addition to the large difference in the spatial resolutions, the data were collected at different times of the day so that they have markedly different illumination geometries. The AVIRIS sensor aboard the NASA ER-2 aircraft provides a good simulation of a satellite-borne imaging spectrometer, whereas the spatial characteristics of the SFSI data set more closely represent those of typical airborne sensor data. In addition to the spatial resolution issue, there is also the issue of atmospheric correction: the AVIRIS data are affected by an air thickness of almost two atmospheres, and the SFSI data by somewhat less. Hence the atmospheric effects must be effectively compensated to retrieve equivalent results. The final issue relates to illumination angles and the effects of shadowing on the final results. This is an important issue when specifying the timing of an overflight, whether it be airborne or satellite-borne.

In this work, radiance data from each of the two data sets are first converted to surface reflectances by correcting for atmospheric effects. A newly developed process is used to automatically extract from these data sets the spectra of the purest pixels, referred to as end members. The hyperspectral data sets are subsequently unmixed using a linear spectral unmixing process to give two sets of end-member "fraction" images. The two sets of end-member spectra are compared to reference spectra to identify the minerals in the target scene so that the corresponding end-member fraction images provide maps for each of the minerals detected at the test site. The two sets of fraction images are compared to determine the degree of agreement between the results derived from the two different remotely sensed data sets. Physical effects that impact the observed spectra and the consequent variances in the fraction images are examined.

Airborne data acquisition

The AVIRIS sensor was flown over the Cuprite, Nevada, target site in the NASA ER-2 aircraft on 12 June 1996 at 1931 UTC (coordinated universal time) at an altitude of 20.1 km above sea level (asl). The nominal ground elevation for the AVIRIS scene is 1.524 km, giving a mean flight altitude of 18.58 km above ground level (agl). The AVIRIS data so acquired cover the whole region surrounding Cuprite. The across-track pixel centre spacing is 16.2 m; comparison with a 1 : 24 000 scale topographic map of the area indicates an along-track line spacing of 18.1 m. The solar zenith angle was 15.85° and the azimuth angle 152.9°. AVIRIS collects data in 224 bands covering the range from 370 to 2508 nm, with a nominal band centre spacing of 10 nm.

The SFSI data used in the analysis reported in this paper were collected on 21 June 1995 over a site located 1.7 km north of the point indicated on the topographic map as Cuprite and cover a relatively small part of the AVIRIS scene. The nominal mean ground elevation for the SFSI scene is 1.554 km. SFSI was mounted in an Aero Commander 500 and flown at an altitude of 3000 m agl at an aircraft speed of 75–80 m·s⁻¹. This gave an along-track sampling interval of 1.5 m and an across-track pixel spacing of 1.0 m. The coordinates of the centre of the SFSI scene are 37°32'38"N and 117°11'2"W, and the time of acquisition was 2382 UTC. The solar zenith angle was 52.39° and the azimuth angle 272.4°. For the data set used in the work reported on in this paper, SFSI collected data in 115 contiguous bands over the range 1219–2405 nm, with a nominal band spacing of 10 nm. This mission was in fact a sensor test flight, only its second, and as such did not entail the acquisition of any ancillary data, e.g., aircraft attitude and coincident radiometric ground referencing. Other data sets acquired on the 1995 SFSI mission in Nevada include imagery acquired near Virginia City

(Hauff et al., 1996; Neville et al., 1997). SFSI has since been modified to reduce the spectral sampling interval to 5 nm, giving 231 bands over the same spectral range, and to increase its FOV from 9.4° to 33.0°.

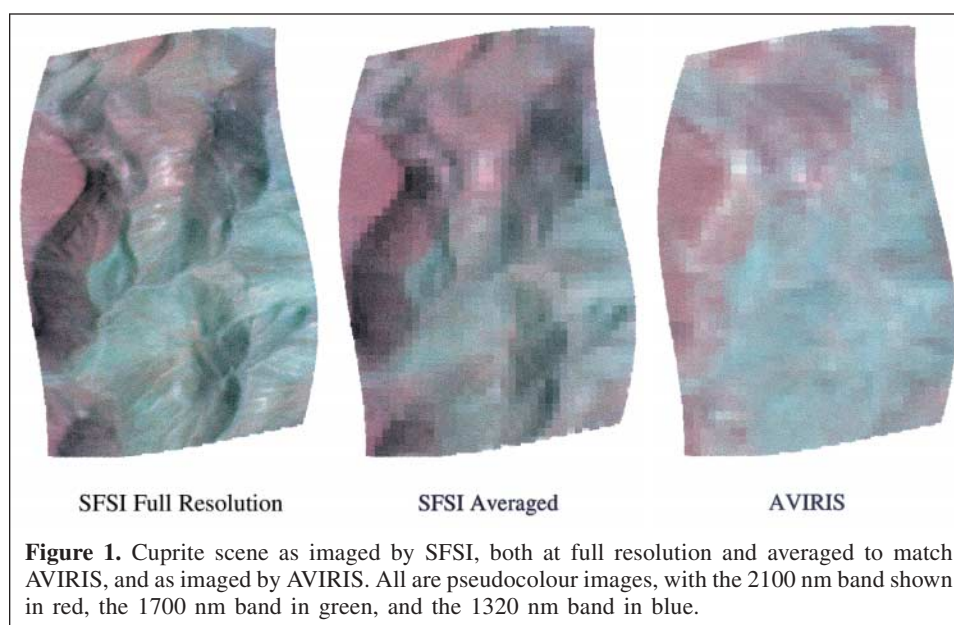
Images of the site covered by the SFSI instrument are displayed in **Figure 1**. From left to right, the first is the full-resolution SFSI image, the second is the SFSI image resampled to match the AVIRIS resolution, and the third is the AVIRIS image. All are pseudocolour images with the 2100 nm band shown in red, the 1700 nm band in green, and the 1320 nm band in blue.

Data processing

Conversion from radiance to surface reflectance

The data used in this analysis had been converted previously from raw sensor signals to radiances. These at-sensor radiances were then converted to surface reflectances. The surface reflectance retrieval procedure implemented in the CCRS Imaging Spectrometer Data Analysis System (ISDAS) uses a six-dimensional linear look-up table (LUT) approach with tunable breakpoints to provide additive and multiplicative coefficients for removal of scattering and absorption effects (Staez and Williams, 1997). The six dimensions are wavelength, surface reflectance, water vapour content, aerosol optical depth, terrain elevation, and view angle. This procedure has the advantage of significantly reducing the number of radiative transfer (RT) code runs and is thereby less time consuming than running such a code on a pixel by pixel basis.

For the LUT generation for the Cuprite data, the MODTRAN3 RT code (Anderson et al., 1995) was run for two different flat reflectance spectra ($\rho_1 = 5\%$ and $\rho_2 = 60\%$), an aerosol optical depth covering the prevailing atmospheric



conditions, and a fixed terrain elevation averaged over the scene. For the SFSI data, a fixed value of water vapour content ($0.6 \text{ g}\cdot\text{cm}^{-2}$) was chosen to best compensate for the absorption features located in the wings of the two major water vapour bands, which are centred at approximately 1400 and 1900 nm. Because the AVIRIS spectral range covers two non-opaque water vapour absorption bands, at 940 and 1135 nm, a fitting routine (available in ISDAS) was used to calculate the total atmospheric water vapour content for each pixel (Staez and Williams, 1997). The calculations made on the RT code wavelength grid were performed at five different pixel locations across the swath for each sensor to encompass the respective sensor geometry. The final step involved in the LUT generation is the convolution of the model output radiances with the relative spectral response profiles for each of the two sensors.

The next processing stage performs an empirical correction for irregularities in the reflectance data that may have originated in the sensor and escaped correction in the processing from raw to radiance data, or that may have resulted from the approximations made in the atmospheric modelling, the selection of input parameters, and the RT calculations. A modified “flat target” procedure (Staez et al., 1999) was used for these data sets. This involves the identification of those image spectra that are the least variable spectrally; then from the ensemble of these spectra, adjustments to the gain and offset are derived for each spectral band. This procedure assumes only that the sought-for spectra are slowly varying, not that they are spectrally flat. This process is implemented in ISDAS.

Co-registration of the images

To assist in the visualization, the SFSI image was transformed using a third-order affine transformation based on a set of 55 ground control points (GCP) found to be common to both images. Neither image has been georeferenced. It was assumed that the AVIRIS image would have fewer aircraft-induced distortions because the high-altitude ER-2 is a more stable platform than the low-flying Aero Commander; hence the SFSI image was mapped onto the AVIRIS image. The AVIRIS image aspect ratio was adjusted to correct for the along-track to across-track pixel spacing difference noted in the Airborne Data Acquisition section. The indicated root mean square (RMS) registration errors among the 55 GCPs are 6.5 SFSI pixels across track and 2.4 SFSI pixels along track. These GCP registration errors translate to 0.50 and 0.22 AVIRIS pixels across track and along track, respectively. By comparison of the AVIRIS and transformed SFSI images, it was determined that, for the area covered by the SFSI image, the AVIRIS pixels were equivalent to 13 transformed SFSI pixels in width and 11 SFSI pixels in length, on average.

These geometric transformations were performed only on the display and output images, i.e., the RGB and fraction images. All spectral analyses were performed on the original

non-transformed data, so the spectral characteristics of the data were not compromised.

Extraction of end-member spectra

Prior to the unmixing operation, one must extract from the set of all spectra contained in the image cube those spectra that come closest to representing pure target materials. Once these “purest” spectra, the end members, have been selected, the unmixing operation is undertaken under the assumption that all the spectra in the data set can be simulated by an appropriate linear combination of the end-member spectra. A note of caution: implicit in this technique is the assumption that no pure material has a spectrum that can be synthesized by a linear combination of the spectra of other pure materials, i.e., that the end-member spectra make up a linearly independent set of vectors in spectral space. This same caveat applies equally to all other methods for identifying mixed targets.

Many techniques for selecting these end members require close operator supervision. This is acceptable when the data volumes are manageable, as in a research project, but for operational survey use such a procedure will become too time consuming to be viable. A number of automatic methods have been investigated (Szeredi et al., 2003) and developed. One of these, the Iterative Error Analysis (IEA) method, has proven to be robust and was used in the analysis of these data sets. The advantages of this method, compared to the operator-guided technique, are that it is more objective, it is more thorough, and it selects end members in order of priority gauged by their relevance in minimizing errors in the unmixed images. One of the potential pitfalls of such a technique is the acquisition of end members from materials contained within the scene, but which are not generally mixed into the pixels of interest. This is the case if cultural objects, such as buildings, are located in the overall scene. These may cause a problem if any of the spectra of such end members were sufficiently similar to one of the desired end members that it is able to substitute for the latter in the unmixing process. These “artifact” end members are best excluded from the data used in the end-member extraction process, either by cropping or by masking those pixels recognized spectrally or spatially as artificial materials or objects.

In general, throughout the analysis of AVIRIS and SFSI data sets, an attempt was made to apply the identical processes to each. However, differences in pixel size and swath width forced slightly different approaches in the end-member extraction procedure. The preferred approach would have been to select the end members from the identical target areas in the two images. However, because of the large size of the AVIRIS pixels (in area, approximately 140 times the SFSI pixel), it would be improbable that any pure pixels would be found among the approximately 1900 AVIRIS pixels covering the same small area as that imaged by SFSI. This is because the larger the pixel, the more likely it is mixed. In part, this is compensated in this case by using the larger AVIRIS scene containing the SFSI scene region and covering an area 160

times that of the SFSI scene. This increased the probability of finding pure pixels for use as end members.

For extraction of the end-member spectra from the AVIRIS data set, the whole 614 pixel by 512 line image cube was used. Twenty-eight end members were acquired (**Table 1**). Of these, 25 are recognizable mineral spectra, one is the “shadow” end member, and two remain unidentified. Only one originated in the area covered by the SFSI scene. All the others came from the remainder of the full AVIRIS scene, and of these some were unimportant in the unmixing of the area coincident with the SFSI scene.

The SFSI image data were convolved with a three by two boxcar kernel, averaging the data spatially to reduce the probability of finding an end member distorted by noise. This gave an effective instantaneous field-of-view (IFOV) of 3 by 3 m. This data set will be referred to subsequently as the “full-resolution” SFSI image. Thirteen end members were extracted from the SFSI data set (**Table 1**). Fewer end members were required for the SFSI scene simply because this limited area contained a smaller variety of minerals than did the larger AVIRIS scene. End members from each of the two data sets were identified as mineral spectra by matching them with spectra acquired in a survey of the general area made with a portable infrared mineral analyser (PIMA) field instrument. Most important for the area covered by the SFSI scene were the alunite, buddingtonite, kaolinite, and opal end members. The end-member spectra of these minerals extracted from the AVIRIS and SFSI scenes and for the PIMA samples are plotted in **Figure 2**.

Unmixing

Linear constrained unmixing was used for this investigation. “Constrained” means that each fraction was required to lie between 0 and 1, and that the sum of the fractions for a given pixel be equal to unity. Such a procedure generally results in larger unmixing errors, i.e., differences between the synthesized

Table 1. Identified minerals and their corresponding end members.

| Spectrum identification | AVIRIS end members | SFSI end members |
|---------------------------|-----------------------|------------------|
| Alunite | 4, 14 | 3, 13 |
| Buddingtonite | 6 | 6 |
| Calcite | 5 | |
| Dickite | 8 | |
| Gypsum | 13 | 10 |
| Illite | 7, 16, 18, 20, 25, 26 | |
| Jarosite | 22 | |
| Kaolinite | 3 | 4, 9, 12 |
| Opal | 1, 9, 12, 19 | 1, 5, 11 |
| Smectite | 10, 17, 21 | |
| Dickite–alunite mixture | 23 | |
| Kaolinite–alunite mixture | 11, 27 | 8 |
| Desert varnish | 24 | 7 |
| Shadow | 2 | 2 |
| Unknown | 15, 28 | |

spectrum and the measured one, than does an unconstrained procedure. However, the latter can, and often does, yield unphysical results, e.g., fractions greater than 1, or indeed negative fractions. Erroneous results can also arise from constrained unmixing if the wrong end members are selected for the unmixing process; the process will always do its best to fit the end-member spectra to the measured spectrum regardless of what those end-member spectra are. It is therefore important that the end members accurately represent the materials in the target site. It is our contention that the most reliable way to guarantee this is to select the end members from the scene under consideration, and to do it as systematically and objectively as possible.

The whole AVIRIS image cube was unmixed using the 28 end members extracted as described previously. Thirty spectral bands covering the range 2059.7–2348.9 nm were used in the linear constrained unmixing process; this spectral range was selected as being the most appropriate for distinguishing the minerals of interest. The SFSI image cube was processed twice: first using the full-resolution SFSI image cube, and second using SFSI data that were averaged in blocks of 13 pixels by 11 lines to simulate the AVIRIS pixels. These two data sets were unmixed using the 13 SFSI end members limited to the 27 bands covering the range 2051.6–2315.3 nm.

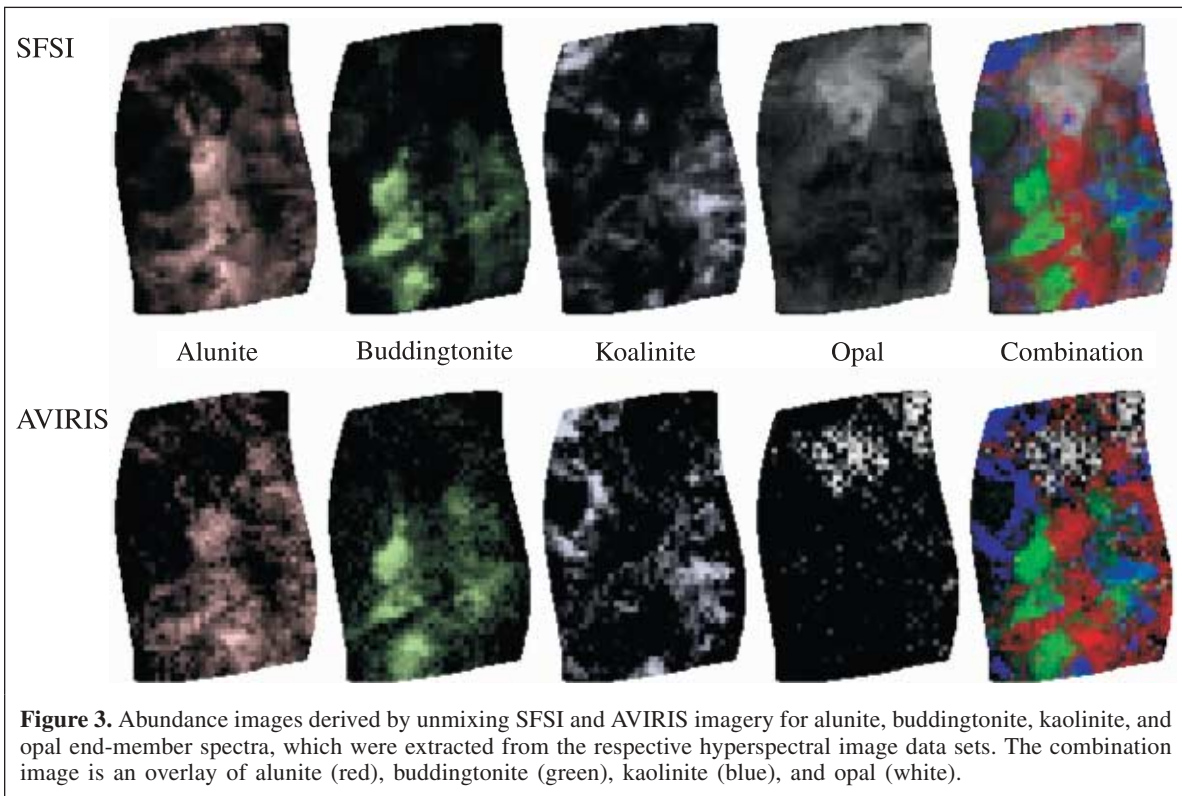
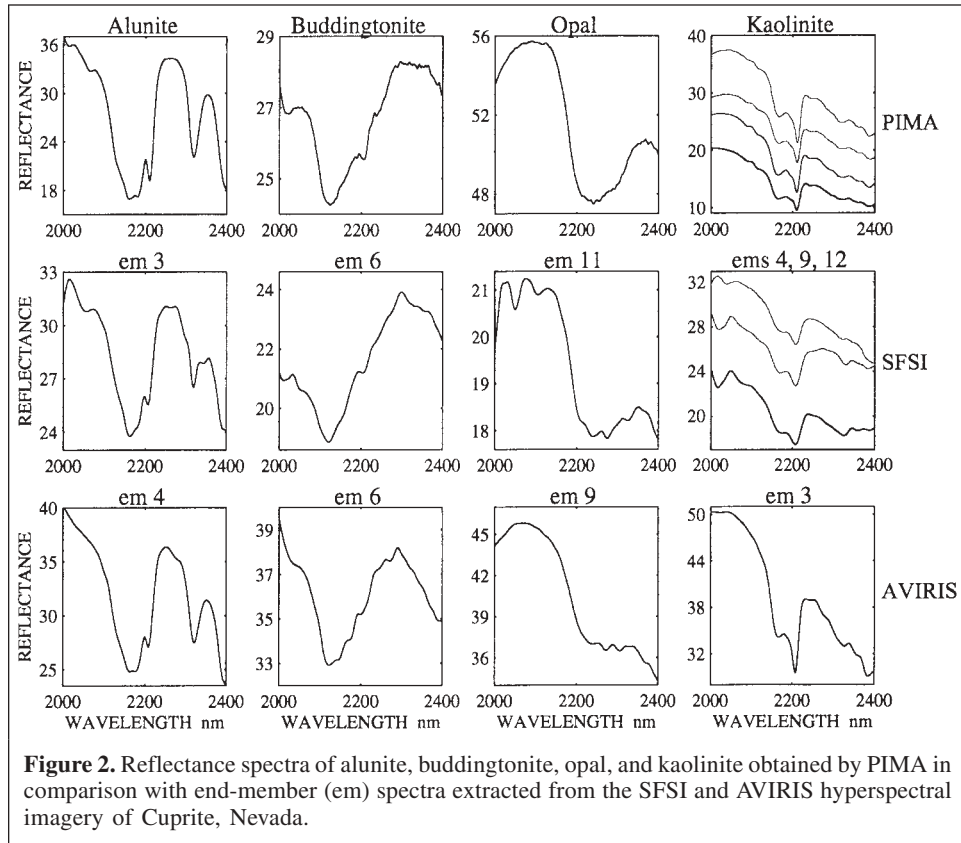
In **Figure 3** the unmixing fractions for alunite, buddingtonite, kaolinite, and opal are displayed both in individual fraction images and in a combination image with the four minerals displayed respectively in red, green, blue, and white, with intensity proportional to fraction value. In the top row are the averaged SFSI fraction images, and in the bottom row are the AVIRIS fraction images masked to show only the area coincident with the SFSI scene.

Statistical analysis

The mineral-fraction images obtained from the two data sets were compared statistically by performing a linear regression of the fraction values for the AVIRIS data against the corresponding values for the averaged SFSI data. This was done on a pixel basis for each of the four minerals alunite, buddingtonite, kaolinite, and opal. The results are listed in **Table 2**.

For these analyses, the fraction data from both AVIRIS and SFSI were renormalized to minimize the impact of the differences in the amount of shadow present in the two data sets. This renormalization was achieved by dividing each of the non-shadow fractions by $(1 - \text{shadow fraction})$. As well, the regression and correlation analyses were performed for both the whole image and for only the set of “bright” SFSI pixels, where the bright pixels have reflectances at or above the mean in the 2200 nm region of the spectrum. The latter was an effort to determine whether there was a significant loss of correlation resulting from the reduced signal-to-noise ratio (S/N) accompanying the lower measured signal for the darker pixels.

In addition, to determine the effects of an inaccurate registration of the SFSI image to the AVIRIS image, the



Pearson's correlation coefficients were calculated for the averaged SFSI fraction images versus the same images that had been shifted by amounts equal to the GCP registration errors of

± 0.5 AVIRIS pixels across track and ± 0.22 lines along track, as noted in the section Co-registration of the images. The same was done for the AVIRIS image, and the geometric mean of

Table 2. Correlation of AVIRIS versus SFSI mineral fraction images.

| Mineral | Correlation coefficient | | Linear regression | | | |
|---------------|-------------------------|---------------|-------------------|---------|---------------|---------|
| | Whole image | Bright pixels | Whole image | | Bright pixels | |
| | | | Slope | Offset | Slope | Offset |
| Alunite | 0.5828 | 0.7185 | 2.2605 | -0.0561 | 1.7793 | -0.0419 |
| Buddingtonite | 0.7421 | 0.8033 | 1.7096 | 0.0274 | 1.4404 | 0.0280 |
| Kaolinite | 0.4880 | 0.6410 | 0.8335 | 0.0374 | 0.7565 | 0.0224 |
| Opal | 0.5928 | 0.6233 | 0.5580 | -0.0051 | 0.5705 | -0.0191 |

Note: The SFSI images are those in which the full resolution results have been averaged to simulate the lower resolution AVIRIS image data.

Table 3. Correlation of AVIRIS and SFSI fraction images versus the corresponding shifted images.

| Mineral | Correlation coefficient | | | | Geometric mean of autoshifted correlation coefficients | |
|---------------|-------------------------|---------------|---------------------------|---------------|--|---------------|
| | SFSI shifted vs. SFSI | | AVIRIS shifted vs. AVIRIS | | Whole image | Bright pixels |
| | Whole image | Bright pixels | Whole image | Bright pixels | | |
| Alunite | 0.8798 | 0.8832 | 0.7986 | 0.7930 | 0.8382 | 0.8369 |
| Buddingtonite | 0.8881 | 0.8898 | 0.8829 | 0.8760 | 0.8855 | 0.8829 |
| Kaolinite | 0.8387 | 0.8442 | 0.7616 | 0.7858 | 0.7992 | 0.8145 |
| Opal | 0.9263 | 0.9417 | 0.7277 | 0.7300 | 0.8210 | 0.8291 |

Note: The SFSI images are those in which the full resolution results have been averaged to simulate the lower resolution AVIRIS image data.

these two sets of autocorrelation coefficients was calculated. These results are listed in **Table 3**. As a measure of what might be expected for the correlation between the SFSI and AVIRIS fractions, had misregistration not been a factor, the SFSI versus AVIRIS correlation coefficients were normalized to these mean autocorrelation coefficients. These are listed in **Table 4**.

Spatial resolution effects

While the loss of spatial detail in going from the SFSI image to the AVIRIS image is evident in **Figure 1**, it is important to determine what impact this has on the detection of mineral outcrops. To show the resulting effects, a small segment of the SFSI fraction image for each of the minerals alunite, buddingtonite, and kaolinite is displayed in **Figure 4** in full resolution and, for comparison, in averaged mode. These image segments are displayed using a colour map to indicate fraction value, with 0 represented by dark blue and 1 by dark red.

Discussion

End-member spectra

The IEA automatic end-member extraction procedure allows the search process to continue until one achieves a desired fidelity level, as represented by the mean unmixing error, which is the relative deviation between the measured pixel reflectance and the reflectance synthesized by a best-fit combination of all the end members. In the present case, it was necessary to acquire 28 end-member spectra to reach a mean unmixing error of 0.56% for the whole AVIRIS scene and 0.54% for that part of the scene coincident with the SFSI scene. This process could

Table 4. AVIRIS versus SFSI correlation coefficients normalized to the mean autoshifted correlation coefficients.

| Mineral | Whole image | Bright pixels |
|---------------|-------------|---------------|
| Alunite | 0.6953 | 0.8585 |
| Buddingtonite | 0.8380 | 0.9099 |
| Kaolinite | 0.6106 | 0.7871 |
| Opal | 0.7220 | 0.7518 |

Note: The SFSI images are those in which the full resolution results have been averaged to simulate the lower resolution AVIRIS image data.

have been curtailed at 24 end members to represent adequately the SFSI subscene. This is not to say that 24 end members were required for the SFSI subscene, but because the whole AVIRIS scene was being searched, and this larger scene contained a greater variety of minerals than did the subscene, the 24 end members were required. The 24th end member was needed to represent the weathered rock predominant in the crescent-shaped plateau area in the upper left edge of the images in **Figure 1**. Lists of the minerals identified and the corresponding end-member numbers are contained in **Table 1**. All but three of the AVIRIS end-member spectra have been identified as mineral targets: one of the three is shadow, and the other two exhibit features not normally associated with mineral spectra and may represent unidentified cultural artifacts in the image. There are duplicate end-member spectra for alunite, illite, opal, and smectite. These differ both in secondary spectral features, which may be caused by the presence of varying amounts of other minerals in the source pixels, and in overall amplitude, which may result from degree of weathering and local terrain slope relative to the solar direction. These and other effects are addressed in the following discussion.

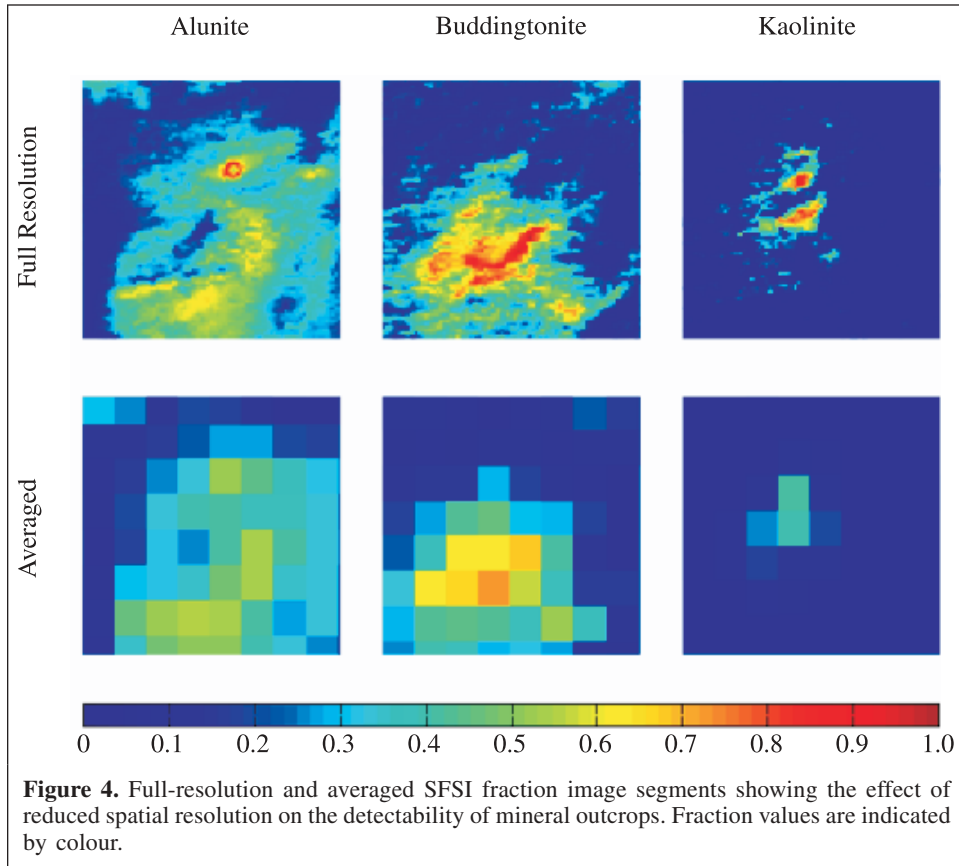


Figure 4. Full-resolution and averaged SFSI fraction image segments showing the effect of reduced spatial resolution on the detectability of mineral outcrops. Fraction values are indicated by colour.

For the SFSI data, 13 end members were sufficient to reduce the mean unmixing error to 1.2% for the full-resolution image cube and 0.66% for the averaged cube. The SFSI end-member spectra have all been identified (**Table 1**). As in the AVIRIS case, there are duplicate representatives, in this case for alunite, kaolinite, and opal. The three kaolinite spectra differ both in amplitude and by the depth of an absorption feature near 2320 nm, which probably indicates the presence of alunite in the selected pixels. The alunite spectra differ markedly in amplitude, and to a minor extent in the width of the feature at 2320 nm. The opal spectra differ in overall amplitude and in the relative depth of the broad absorption feature spanning 2200–2300 nm, both of which may be the result of the effects of particle-size distribution, as discussed in the next paragraph. In addition, both the AVIRIS and SFSI data sets produce end-member spectra that are readily identified as mixtures of kaolinite and alunite.

For any dielectric material the reflectance is affected by the number of reflecting surfaces per unit volume. The larger this number, the greater will be the backscatter of the incident radiation, and the brighter the target will appear. Hence, a target consisting of a distribution of particle sizes in which the finer components dominate will have a higher observed reflectance than one with a coarser distribution. This also applies to crystals containing fracture surfaces; those with a higher concentration of fractures will have higher effective reflectances. The particle-size distribution, or the fracture surface density, will also have

an impact on the observed depth of any spectral absorption feature exhibited by a given material. The greater the path length of the radiation in the interior of the particle, the greater will be the amount of absorption characteristic of that particular material. For radiation incident upon an aggregate of particles, the effective path length in the interior of the particles before it is scattered back toward a sensor, for example, is greater when the particles are larger and have fewer fracture surfaces. The net result is that the coarser particle distributions will have lower overall reflectance but more prominent absorption features.

The site covered by the SFSI image consists predominantly of opal, alunite, buddingtonite, and kaolinite. For these minerals the AVIRIS and SFSI end-member spectra and the PIMA field sample spectra, shown in **Figure 2**, correlate sufficiently well that the end-member spectra can be readily identified as the corresponding minerals. There are some differences that will be discussed here.

The PIMA instrument contains its own light source that irradiates the small (approximately 20 mm²) area viewed by the detector at close proximity to the target sample. Because of its particular viewing geometry relative to the irradiating geometry, there are few if any shadows, even at a microscopic scale, resulting from any inherent surface roughness. By comparison, a passive remote sensor, i.e., one that depends on natural radiation, almost always views the scene at an angle relative to the incident irradiance, which guarantees that the

detector sees a partially shaded scene. Whether the shadows are resolved spatially by the sensor depends on the scale of the surface roughness relative to the detector's ground IFOV (GIFOV); regardless, the resulting measured reflectance will be lower than it would had the viewing direction been aligned exactly parallel to the incident irradiance. In remote sensing and astronomy this dependence of the apparent reflectance on the viewing direction relative to the irradiance direction is known as the bidirectional reflectance or "phase angle" effect (Egan 1985). The peaking of the reflectance for the situation where the reflected radiance is directed back toward the source is called the "opposition effect". In aerial photography this same effect results in the "hot-spot" phenomenon.

One would, on this basis, expect the PIMA reflectances always to be higher than those derived from the airborne sensor data. However, we must also note that there are considerable differences in the overall reflectances of the same mineral even as seen with the PIMA survey (**Figure 2**). These differences can be caused by weathering or the presence of other materials in the sample that have a lower reflectance but are spectrally undistinguished. The AVIRIS end-member spectra exhibit, for the most part, greater reflectances than do the corresponding SFSI spectra and, indeed, even more than some of the PIMA spectra. It is noted that the conversion from radiance to reflectance assumed that the terrain was flat and that the surface of all pixels is horizontal. In reality there is significant topographical relief in the target area that results in localized variations in the surface slopes. Those pixels sloping toward the sun will appear brighter than those which are horizontal or sloping away from the sun and, because this is not compensated for in the reflectance derivation, the calculated reflectances can be too high for individual pixels. It is suggested that this is more likely to be the case for the AVIRIS data set than for the SFSI data set. The AVIRIS data were acquired with a high solar elevation (solar zenith angle = 15.85°), whereas the SFSI data were acquired with a relatively low sun angle (solar zenith angle = 52.39°). Terrain slopes sufficient to result in pixels with surfaces orthogonal to the solar direction are much more probable for the AVIRIS data (15.85°) than for the SFSI data (52.39°), although the latter may in fact occur in this scene. Thus, the terrain slope effects are likely to result in an overestimation of the reflectances for the AVIRIS data set. Compounding the problem is the fact that the end-member extraction process selects the brightest examples for each of the spectrally distinct pixels, hence preferentially selecting a reflectance spectrum that may be so brightened. Conversely, there is a lower probability that the SFSI end-member pixels will have the advantage of optimally oriented surfaces. This, combined with the increased likelihood that shadow is present in all the pixels, a result of the low sun elevation, implies that the reflectances of the SFSI end members are more likely to be underestimated.

In addition to these geometric effects, there can be slight variations from sample to sample in the composition of a given mineral, possibly with the admixture of other dark but spectrally nondescript materials that affect its overall

reflectance. See, for example, in **Figure 2** the four PIMA kaolinite spectra all acquired from samples in the Cuprite area and note the three kaolinite spectra that emerge as end members from the SFSI data.

There are also a number of differences from sensor to sensor in the shapes of the spectra. These can result for a variety of reasons. The composition and degree of weathering of the various samples for a given mineral can vary. Such differences have already been noted in spectra obtained by a single sensor for a given mineral. The same factors apply when comparing spectra from different sensors. It is known that in general the SFSI and AVIRIS end-member spectra came from different target locations, and there has been no attempt in the current work to coordinate the precise locations of the PIMA samples with the respective airborne spectral measurements, only that the PIMA samples came from the Cuprite area. In addition, sensor noise, uncertainties in radiometric calibration, and inadequacies in the atmospheric correction can lead to differences in the spectra obtained by the different sensors. The low solar elevation angle for the SFSI acquisition reduces the S/N for this data set, which leads to potentially higher errors in the atmospheric correction. It is known from in situ observation that the opal sample in the SFSI scene is located on a slope that is tilted away from the sun. This results in both a reduction, by at least a factor of two, for the SFSI opal end member as compared with the opal spectra acquired by PIMA and AVIRIS, and also an increased potential that noise may distort the spectrum.

The differing techniques used for the atmospheric water vapour correction may also be contributing to the differences in shapes of the AVIRIS and SFSI spectra. As has been noted, the AVIRIS data set was corrected on a pixel by pixel basis by using the 940 and 1135 nm water vapour bands to determine the water vapour content. By contrast, the SFSI data set was processed using a constant $0.6 \text{ g}\cdot\text{cm}^{-2}$, a value arrived at by an approximate method that implicitly assumes that the spectrum of the underlying scene material is flat.

The above points relating to spectral differences arising from slight variations in mineral composition, degree of weathering, and uncertainties in sensor calibration and atmospheric correction can also be used to support the preference for using end members derived from the scene, rather than library spectra. It is sufficient to be able to identify the mineral species corresponding to the end-member spectra. The unmixing results will be correct, even if the derived spectra retain some sensor or processing generated artifacts.

Unmixing fraction images

Visual assessment of **Figure 3**, which contains the fraction images for the four dominant minerals at this site, namely alunite, buddingtonite, kaolinite, and opal, indicates very good agreement between the AVIRIS and the averaged SFSI images. Noted especially is the strong similarity in the interlacing of the patterns of the four minerals in the "combination" pair of images. When a quantitative comparison is made on a pixel by

pixel basis, however, one finds results that are less encouraging (**Table 2**). The question is why the quantitative correlation results are only fair when the visual results are so good. Possible explanations for the decorrelation of the SFSI and AVIRIS results derive from the lower solar elevation for the SFSI image and the lack of sufficient aircraft navigation and attitude reference data to georeference the SFSI image data sufficiently accurately.

Significant shaded areas apparent in the SFSI image (**Figure 1**), which are not present in the AVIRIS data, are the result of the low solar elevation for the SFSI data acquisition. One such area is that along the southeast boundary of the crescent-shaped region in the upper left part of the image; it appears dark in the SFSI RGB image, and bright in the AVIRIS image. This area appears as a high kaolinite region in the AVIRIS fraction image, but is absent from the corresponding SFSI fraction image.

In less dramatic cases there are two potential effects on the unmixing results. The first is that the “shade” end-member fraction will be higher, and the remaining “mineral” end-member fraction values will be lower, for the SFSI pixels that fall in the shadowed regions. This results in higher mineral-fraction values for the AVIRIS data than for the corresponding SFSI pixels. In an attempt to compensate for this possible effect, the unmixing fraction values have been renormalized (see the Statistical analysis section) on a pixel by pixel basis by dividing by $(1 - \text{shade fraction})$. The data for which the correlation results are shown in **Table 2** have already been subjected to such a renormalization, for both SFSI and AVIRIS. However, there may be residual effects remaining after the renormalization that result from the fact that the SFSI and AVIRIS shade spectra are neither flat nor spectrally similar to each other. Hence the effect of a high shade fraction will be mineral dependent, and this dependence will be different for the two data sets. This renormalization is therefore only a first-order correction for this effect.

The second consequence of the low sun angle is a lower sensor signal level and hence a lower S/N for those pixels with significant shade fractions. The end-member fraction values derived from these low S/N spectra will have higher error levels. This is corroborated by the results in **Table 2** that indicate that the bright pixel data sets correlate more favourably than do the “whole image” data sets.

The fact that neither the SFSI nor the AVIRIS images were georeferenced made it impossible to do an accurate image to image registration. The effect of a representative misregistration on the correlation of the fraction images is shown in **Table 3**. Displayed here are the results of correlating each of the AVIRIS and averaged SFSI images with itself, after first shifting the image by ± 0.5 AVIRIS pixels across track and ± 0.22 lines along track, as described in the Statistical analysis section. It is observed that even this modest degree of misregistration results in a notable decorrelation of the fraction images. **Table 3** contains for each of the SFSI and AVIRIS images, and separately for the set of all the pixels and for the set of bright pixels, the means of the autocorrelation coefficients for the four

combinations of shifts specified previously. Also listed are the geometric means of the SFSI autocorrelation coefficients with the corresponding AVIRIS coefficients. When the AVIRIS versus SFSI correlation values are “normalized” to these geometric means of the autocorrelations for the shifted images, the resulting values range from 0.75 to 0.91 for the bright pixel data sets (**Table 4**). Although this “normalization” cannot be considered a rigorous correction for the impact of the image misregistration, it does provide an improved estimate of what might be expected had accurate registration of the images been possible.

Another observation that can be made from **Table 2** is that the linear regressions give slopes that range from 0.57 for opal to 1.78 for alunite, for the bright pixels, and from 0.56 for opal to 2.26 for alunite when all pixels are included. This indicates that the AVIRIS data set gives higher fraction values for alunite and buddingtonite, and SFSI gives higher values for kaolinite and opal. It is suggested that this results in part from the use of the whole AVIRIS image as the data set from which to extract the AVIRIS end-member spectra. As discussed in the previous section, the AVIRIS end-member spectrum for a given mineral may have a different amplitude than the corresponding SFSI end-member spectrum, and these amplitude differences may vary from mineral to mineral, depending on purity, weathering, and local illumination conditions of the end-member source pixel. The greater the amplitude of a given end-member spectrum, relative to the mean amplitude of the whole set of end members used in the unmixing, the smaller will be the mean fraction value for that particular end member. This is corroborated by the results of a correlation analysis comparing the linear regression slopes of **Table 2** with the ratios of the relative end-member spectra amplitudes for AVIRIS to those for SFSI.

This analysis proceeded as follows. For each of the two image data sets, the end-member spectra amplitudes were divided by the mean amplitude for the whole set of end members used in unmixing the corresponding data set. This resulted in “group-normalized” amplitudes for all the end members in each of the two sets. Next, the ratios of the group-normalized SFSI amplitudes for the alunite, buddingtonite, kaolinite, and opal end members to the corresponding AVIRIS amplitudes were calculated. It was found that these ratios correlate with the linear regression slopes of **Table 2**, with a correlation coefficient of 0.76.

This result highlights the fact that different fraction values will be obtained depending on the source(s) of the spectra used in the unmixing operation. In the present case, AVIRIS spectra were used to unmix the AVIRIS scene, and SFSI spectra to unmix the SFSI scene. The differences encountered here result solely from the selection of different end-member source locations within the respective scenes. If library spectra, acquired by sensors with different measurement characteristics, viewing minerals with conditioning and illumination different from those in the scene, were used for the end-member spectra, then one could expect even greater disagreements in fraction values.

Spatial resolution

A comparison of the full spatial resolution SFSI fraction images in **Figure 4** with the corresponding spatially averaged images shows that the degree of information loss depends on the scale and intensity of the target feature. For the alunite image “swatch” it is observed that the averaged or low-resolution image adequately represents most of the scene, where the fraction values remain roughly constant over areas comparable in size to the larger pixel IFOV. However, the low-resolution image fails to highlight adequately the highest concentration outcrop of this mineral because its spatial extent is less than that of the pixel IFOV. For the buddingtonite image swatch, the low-resolution representation performs better because the spatial distribution of the mineral outcrops is less disjoint. The low-resolution imagery performance is poorest for the kaolinite sample image, where the high-purity outcrops are each approximately one-half pixel in size but are embedded in a low-intensity background. For this case there is a high risk that this outcrop would be ignored in the context of a large survey image set. In all cases much of the information regarding the mineral distribution within the outcrops is lost in the low-resolution data. This has a significant impact on the degree of effort required to validate these remotely sensed data with ground sampling. The area that one must sample is correspondingly larger, and because there are significant fraction variations down to at least the 1 m level, as evidenced by the full-resolution SFSI image, it is not sufficient to perform only a small number of ground measurements per 20×20 m pixel.

Summary and conclusions

Two hyperspectral image data sets collected in successive years over the same Cuprite, Nevada, site by different airborne imagers have been analysed and the results compared. One data set collected by SFSI in 1995 imaged an area of 0.50 by 0.84 km with pixels on 1.0 by 1.5 m centres; the other collected in 1996 by AVIRIS imaged an area of 9.95 by 9.27 km with pixels on 16.2 by 18.1 m centres. The SFSI scene is contained within the much larger AVIRIS scene. Both sensors have nominal spectral band widths and band centre spacings of 10 nm. The principal difference in the scene on the two dates was the solar zenith angle, which was 52.39° for the SFSI scene and 15.85° for the AVIRIS scene. As a result, the former contained large areas of deep shadow, whereas the same region in the latter scene contained no significant shadow. Both data sets were converted from at-sensor radiances to surface reflectances via an atmospheric correction process incorporating the MODTRAN3 RT code implemented on ISDAS.

The IEA procedure was used to extract a set of end-member spectra from each of the two data sets. By comparing these end-member spectra with in situ PIMA measurements and library spectra, nearly all were identified as specific mineral spectra, with some being mixtures of pairs of minerals. Despite the differences in spatial resolution, areal coverage, and

illumination conditions, there is a very good correspondence between the SFSI end-member spectral signatures and those of the end members of the AVIRIS set that represent materials present in the SFSI subscene. The linear constrained unmixing analyses of the two image data sets gave results that are generally in agreement with respect to the mineral composition of the scene covered by the SFSI image. Particularly striking is the similarity in the spatial interlacing of the distributions of the most abundant four minerals, namely alunite, buddingtonite, kaolinite, and opal. This agreement is sufficient evidence to conclude that the constrained linear unmixing procedure employed in this work is robust, and that one can expect it to produce similar results for a wide variety of hyperspectral data collected under very different illumination conditions. This, coupled with the ability to identify the spectra, is strong evidence to recommend the procedure used to create the mineral-fraction maps. There are, however, some caveats and conditions that must be added.

Observed differences in the amplitudes of the spectra from one end-member set and the corresponding spectra from the other set result, in part, from the very different illumination conditions for the two images. In addition, the locations of the end-member source pixels were different for the two images, primarily because the AVIRIS image covers a much larger region, containing a larger variety of minerals than does the SFSI image. These amplitude differences between the two sets, and more precisely the different intra-set ordering of the amplitudes, result in calculated mineral fractions that disagree, on average, by as much as a factor of two. One should expect even greater disparities if an unmixing procedure were applied using library spectra acquired by sensors having different measurement characteristics, viewing minerals with different conditioning and illumination than those in the scene. The message is that for best fraction accuracies one should take the end-member spectra from the scene under analysis. In addition, one should consider performing a topographic – slope correction on the derived reflectances. Still, variations in surface conditioning will reduce the accuracies of the fraction values.

Observed spectral signature differences between the two end-member sets and between these and the reference library spectra, which may result from varying degrees of success in removing the atmospheric effects and from radiometric calibration errors, have probably less impact on the accuracy of the mineral fraction maps. From this standpoint these effects are less important, provided that the identification of the end-member spectra is not compromised.

The less convincing correlation analysis results comparing the two sets of mineral fraction maps are caused in part by the lack of an accurate registration between the two images, and in part by the strong shading in parts of one of the images. In most practical applications of this mineral mapping technique, image misregistration is not a consideration. However, the loss of accuracy in deeply shaded regions will certainly be a concern, especially in areas of high topographic relief.

With regard to the spatial resolution issue, it is recommended that the IFOV of the sensor be no greater than twice the smallest feature size that one hopes to be able to detect confidently.

Acknowledgements

The SFSI mission in Nevada was funded by the following companies: G.A. Borstad Associates Ltd., Spectral International Inc., Barrick Gold Corporation, BHP Minerals Canada Ltd., Cameco Corporation, Cominco Ltd., CRA Exploration Pty. Ltd., Homestake Mining Company, Newmont Gold Company, North Mining Inc., Placer Dome Exploration, and Western Mining Corporation. Data used in this paper have been provided courtesy of these companies.

References

- Adams, J.B., Smith, M.O., and Johnson, P.E. 1986. Spectral mixture modelling: a new analysis of rock and soil types at the Viking lander site. *Journal of Geophysical Research*, Vol. 91, pp. 8098–8112.
- Anderson, G.P., Wong, J., and Chetwynd, J.H. 1995. MODTRAN3: an update on recent validations against airborne high resolution interferometer measurement. In *Summaries of the Fifth Annual JPL Airborne Earth Science Workshop*, 23–26 Jan. 1995, Pasadena, Calif. Edited by R.O. Green. Jet Propulsion Laboratory Publication 95-1, Vol. 1, pp. 124–133.
- Berk, A., Bernstein, L.S., and Robertson, D.C. 1993. *MODTRAN: a moderate resolution model for LOWTRAN7*. AFGL Technical Report GL-TR-89-0122, Air Force Geophysics Laboratory, Hanscom AFB, Mass. 42 pp.
- Boardman, J.W. 1989. Inversion of imaging spectrometry data using singular value decomposition. In *Proceedings of the 1989 International Geoscience and Remote Sensing Symposium (IGARSS'89) and the 12th Canadian Symposium on Remote Sensing*, 10–14 July 1989, Vancouver, B.C. Vol. 4, pp. 2069–2072.
- Boardman, J.W. 1990. Inversion of high spectral resolution data. In *Proceedings of the SPIE Conference on Imaging Spectroscopy of the Terrestrial Environment*, 16–17 April 1990, Orlando, Fla. Edited by G. Vane. Proceedings of SPIE, Vol. 1298, pp. 222–233.
- Borstad, G.A., Edel, H.R., Gower, J.F.R., and Hollinger, A.B. 1985. Analysis of test and flight data from the fluorescence line imager. *Canadian Special Publication of Fisheries and Aquatic Sciences* 83. 38 pp.
- Egan, W.G. 1985. *Photometry and polarization in remote sensing*. Elsevier Science Publishing Co., Inc., New York. 503 pp.
- Green, R.O., Eastwood, M.L., Sarture, C.M., Chrien, T.G., Aronsson, M., Chippendale, B.J., Faust, J.A., Pavri, B.E., Chovit, C.J., Solis, M., Olah, M.R., and Williams, O. 1998. Imaging spectrometry and the airborne visible/infrared imaging spectrometer (AVIRIS). *Remote Sensing of Environment*, Vol. 65, pp. 227–248.
- Hauff, P., Kowalczyk, P., Ehling, M., Borstad, G., Edmundo, G., Kern, R., Neville, R., Marois, R., Perry, S., Bedell, R., Sabine, C., Crósta, A., Miura, T., Lipton, G., Sopuck, V., Chapman, R., Tilkov, M., O'Sullivan, T., Hornibrook, M., Coulter, D., and Bennett, S. 1996. The CCRS SWIR full spectrum imager: mission to Nevada. In *Proceedings of the 11th Thematic Conference on Applied Geologic Remote Sensing*, 27–29 Feb. 1996, Las Vegas, Nev. ERIM International, Ann Arbor, Mich. Vol. 1, pp. 38–47.
- Neville, R.A., and Powell, I. 1992. Design of SFSI: an imaging spectrometer in the SWIR. *Canadian Journal of Remote Sensing*, Vol. 18, No. 4, pp. 210–222.
- Neville, R.A., Rowlands, N., Marois, R., and Powell, I. 1995. SFSI: Canada's first airborne SWIR imaging spectrometer. *Canadian Journal of Remote Sensing*, Vol. 21, No. 3, pp. 328–336.
- Neville, R.A., Staenz, K., and Szeredi, T. 1997. Mineral reflectances extracted from SFSI imagery in Nevada. In *Proceedings of the SPIE Conference on Algorithms for Multispectral and Hyperspectral Imagery III*, 22–23 April 1997, Orlando, Fla. Edited by A.E. Iverson and S.S. Shen. Proceedings of SPIE, Vol. 3071, pp. 147–157.
- Porter, W.M., and Enmark, H.T. 1987. A system overview of the airborne visible/infrared imaging spectrometer (AVIRIS). In *Proceedings of the SPIE Conference on Imaging Spectroscopy II*, 16–17 Aug. 1987, San Diego, Calif. Edited by G. Vane. Proceedings of SPIE, Vol. 834, pp. 22–31.
- Staenz, K., and Williams, D.J. 1997. Retrieval of surface reflectance from hyperspectral data using a look-up table approach. *Canadian Journal of Remote Sensing*, Vol. 23, No. 4, pp. 354–368.
- Staenz, K., Neville, R.A., Lévesque, J., Szeredi, T., Singhroy, V., Borstad, G.A., and Hauff, P. 1999. Evaluation of *casi* and SFSI hyperspectral data for environmental and geological applications – two case studies. *Canadian Journal of Remote Sensing*, Vol. 25, No. 3, pp. 311–322.
- Szeredi, T., Staenz, K., and Neville, R.A. 2003. Automatic end member selection: theory. *Remote Sensing of Environment*. In press.
- Tanré, D., Deroo, C., Duhaut, P., Herman, M., Morcrette, J.J., Perbos, J., and Deschamps, P.Y. 1990. Description of a computer code to simulate the satellite signal in the solar spectrum: the 5S code. *International Journal of Remote Sensing*, Vol. 11, No. 4, pp. 659–668.
- Tillet, P.M., and Santer, R.P. 1991. Terrain elevation and sensor altitude dependence in a semi-analytical atmospheric code. *Canadian Journal of Remote Sensing*, Vol. 17, No. 1, pp. 36–44.
- Vane, G., and Goetz, A.F.H. 1988. Terrestrial imaging spectroscopy. *Remote Sensing of Environment*, Vol. 24, pp. 1–29.